www.DeepakPublishing.com

Shobha, V. et al. (2017): JoSS, Vol. 6, No. 2, pp. 581–589
(Peer-reviewed article available at www.jossonline.com)

www. JoSSonline.com

Investigation of Gamma and High Energy Electron Dose Effect on a MOEM Sun Sensor Developed for Micro Satellite Applications

S. P. Karanth, V. Shobha, Sumesh M. A., T. V. Sridevi, K. T. Manjunath, Beno Thomas, L. V. Prasad, M. Viswanathan

Laboratory for Electro-Optics Systems (LEOS)
First Phase, First Cross, Peenya Industrial Estate
Bengaluru, Karnataka, India

Abstract

High accuracy micro sun sensors (i.e., with angular resolution better than 0.1°) for space applications are designed and developed using n^+/p junction twin triangular silicon photo detectors (planar process) anodically bonded with micro-optics (Corning 7740) that have an etch cavity depth of around 100 μm on one side and a 300 μm wide slit patterned on high optical density black chrome on the other side. This sensor configuration determines sun angle by taking differential current outputs from the individual photo-detectors. The normalization technique adopted makes the output independent of flux variations, ambient temperature fluctuations, and cosine effect of incidence. Micro sun sensor devices, for which field of view is around ±50°, are characterized for sensor performance, including mainly sensitivity and non-linearity in the linear range of ±25°. Achieved sensitivity and non-linearity of these devices are 140 mV/deg and better than 10%, respectively. In addition, the effect of gamma and electron irradiation on the sensor's performance was studied. Two devices were subjected to gamma radiation (dose = 100 krad), with a rate of 23 *rad/s* using *Co-60* source, with a finding of no gamma radiation effect on sensor voltage output. Post-sensor performance evaluation of the two devices that underwent electron irradiation of energy 8–10 MeV with a fluence of $2\times10^{13}/cm^2$ revealed that sun presence, non-linearity, and sensitivity are varied. The high energy particle irradiation effect was studied with the help of analytical models, and variation was substantiated quantitatively.

1. Introduction

Sun sensors are used in the control and determination of spacecraft attitude. The Laboratory for Electro-Optics Systems (LEOS) has initiated activity to use a micro-electro-mechanical (MEMS) fabrication route combined with planar silicon processing technology for the development of high accuracy, low mass, low volume, miniaturized sun sensors (i.e., micro sun sen-

Corresponding Author: V. Shobha, v_shobha@leos.gov.in

sors) for space applications (Hales et al., 2002; Pederson et al., 2002). A micro sun sensor consists of two parts: an active component (the silicon photo detector) and a passive component (micro-optics made of radiation resistant Corning 7740). Radiation damage is mainly expected in the silicon photo detector, whereas the radiation-hardened glass (the Corning 7740) experiences almost no effect from space radiation (Corning glass, 1987).

Performance of silicon photo detectors is degraded by the cumulative effect of protons and electrons. The particle radiation environment in the vicinity of Earth consists of mostly protons and electrons trapped for long time intervals in the geomagnetic field. At the altitude of geosynchronous orbit, the trapped 1 MeV electron flux is 5×10^{10} particles / cm^2 / day, while the trapped proton flux is negligible. For non-geosynchronous orbit, dose rate variations at different longitudes are averaged out during the day, so that a given total dose corresponds to a specific time interval (Partain et al., 1995). In the present paper, the cumulative effect of 1MeV electron flux on the device is studied as part of space qualification testing and evaluation.

For the silicon photo detector, radiation damage mechanisms are mainly lattice displacement and, to a lesser extent, ionization. Lattice displacement is due to an elastic collision process between the nucleus of a regularly placed atom and an energetic particle, causing the atom to move into an interstitial position and forming defect complexes with other defects or with impurities. The ionization process is an inelastic process whereby an atomic electron gains sufficient energy from a collision and becomes unbounded (Partain et al., 1995; Mazer, 2011). The electron moves from valence band to conduction band and creates electron hole pairs (EHP) (Partain et al., 1995; Karanth et al., 2006). This process is similar to the generation of EHP by an incoming photon. Ionization by collision requires three times the energy of photon absorption. Ionization degradation in the silicon detectors occurs as the electron becomes trapped in the surface oxide or other dielectric (Partain et al., 1995). The effect of gamma and electron irradiation on sensor performances such as sensitivity, linearity, and sun presence is discussed in detail below.

2. Sensor Principle

The working principle of the sun sensor is explained in Figure 1. When the sun rays enter the slit of finite width and illuminate silicon photo detector pixels placed beneath the slit, current is generated in the photo detectors and is given by Eq. 1 (Hales et al., 2002; Pederson et al., 2002):

$$I_t = \frac{(P/A)A_t(\alpha)\cos(\alpha_k)\cos(\alpha_e)(1-\eta)}{V(T)}, \qquad (1)$$

where P/A= sun power per square centimeter at the satellite (mW/cm^2); $A_{t(\alpha)}$ = illuminated area of one triangle (cm^2); $V(T)$ = diode forward knee voltage (V); α_k and α_e = sun rays angles about the k and e axes (^{o}); and η = photo detector quantum efficiency.

The difference between the generated currents in the two triangular photo detectors is normalized. The resultant normalized differential current is used to compute the sun angle and is shown as:

$$\frac{\Delta I_{(\alpha,k)}}{\sum I} = \frac{(I_{t2}-I_{t1})}{(I_{t2}+I_{t1})} = \frac{\{A_{t2}(\alpha)-A_{t1}(\alpha)\}}{\{A_{t2}(\alpha)+A_{t1}(\alpha)\}} \qquad (2)$$

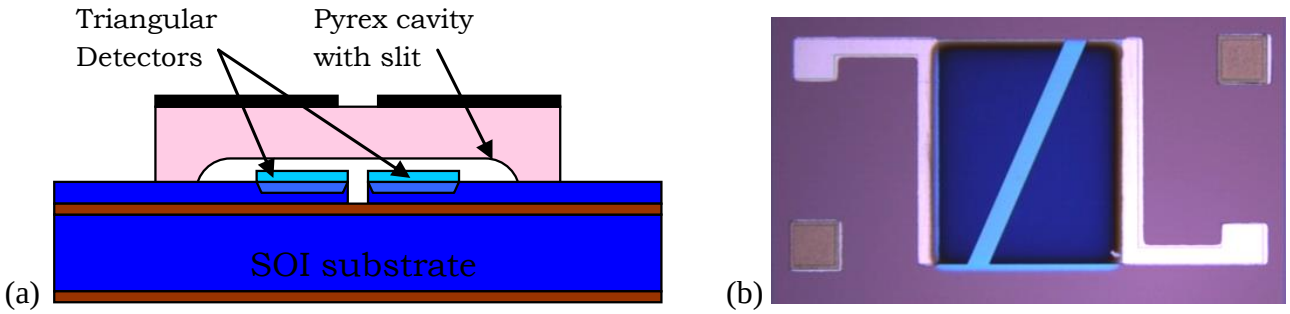

Figure 1.(a) Schematic view of a micro-sun sensor; (b) Photograph of silicon chip showing twin triangular photo detectors.

which indicates that sensor output is only a function of the illuminated areas of silicon photo-detector pixels.

3. Sensor Design

Sensor design is based on the sun presence current signal requirement within a measurement field of view (MFOV) α_k = ± 45° and cross field of view (CFOV) α_e = ±70°. For a chosen sun presence (FOV) signal, output at null (MFOV=0º, CFOV=0º) will be 5µA, which is the sum of two photo currents from each triangular photo detector when illuminated through the slit. The signal current at null is further taken as the base for designing the physical geometry of the triangular detector. The triangular detector height *(k)* is determined by using Eq.1 by setting current value at null:

$$I_{t(null)} = \frac{(P/A)(1/2)ak(1-\eta)(1-R)}{V(T)}, \quad (3)$$

where *R* is reflection *(%)* from the surface of the detector plane:

$$k = \frac{2\, I_{t(null)} V(T)}{a(P/A)(1-\eta)(1-R)}. \quad (4)$$

The triangular detector width *'e'* is designed from required MFOV (α_k = ± 45°), using the tan relationship.

Detector width is given by:

$$e = \left[\tan\left\{\sin^{-1}\left(\frac{\sin\alpha_k}{\mu}\right)\right\}\right](c-l) + (l\,\tan\alpha_k), \quad (5)$$

where α_k, μ, c and l are angle of incident, refractive index of medium, thickness of pyrex glass, and air gap between the detector plane and slit respectively (Shobha et al., 2011).

From Eq. 2, it can be seen that the sensor output depends on $A_{t2}(\alpha)$ and $A_{t1}(\alpha)$. For a case when sun rays enter through a slit mask and illuminate the detector plane, the corresponding illuminated areas $A_{t1}(\alpha)$ and $A_{t2}(\alpha)$ are derived from the geometry of triangular detector, air gap, glass wafer thickness, and law of refraction for propagation of incident sun rays into a medium, and are given by:

$$A_{t1}(\alpha) = \frac{(a-s)(2e+2(c-l)\tan\alpha_o+2l\,\tan\alpha_i+s)\,k}{4e}, \quad (6)$$

$$A_{t2}(\alpha) = \frac{(a-s)(2e-2(c-l)\tan\alpha_o-2l\,\tan\alpha_i-s)\,k}{4e}, \quad (7)$$

In Eqs. 6 and 7, *'a'*, *'α_o'*, and *'s'* are slit width, angle of refraction in the glass medium, and *btan*α_i respectively, where *'b'* is the black chrome coating thickness in the slit mask.

Finally, the sensitivity of the micro sun sensor can be derived by:

$$\frac{(I_a-I_b)}{(I_a+I_b)} = \frac{(-2(c-l)\tan\alpha_o-2l\,\tan\alpha_i-s),}{2e} \quad (8)$$

Eq. 8 was used in the MATLAB simulations to identify the dependence of sensitivity and non-linearity with respect to geometrical parameters of the sensor, namely triangular width, sensor-pyrex distance, etc. Simulated outputs/plots are depicted in Figure 2.

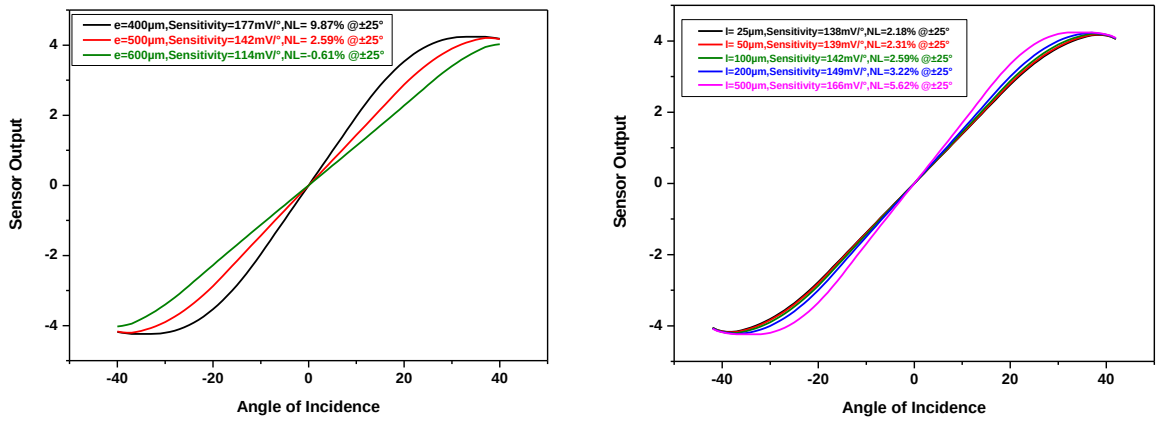

(a) Variation of sensitivity and non-linearity w.r.t. half triangular width (e) (b) Variation of sensitivity and non-linearity w.r.t. air cavity (l)

Figure 2. Variation of sensitivity vs. sun angle incidence in degrees.

Optimization is carried out to obtain required sensor output (~150 mV/deg), considering the trans-impedance amplifier feedback resistance of 1 MΩ, thus providing a gain of 120dB, while the non-linearity is less than 5% within the FOV ±25°. The optimized micro sun sensor dimensions are shown in Table 1.

Table 1. Optimized Micro Sun Sensor Dimensions

Sensor geometrical parameter	Optimized Values
Slit width, *a*	300 μm
Slit extra length, *g*	1250 μm
Slit length	5800 μm
Triangle height, *k*	2800 μm
Triangle width, *2e*	1000 μm
Pyrex thickness, *c*	1000 μm
Air cavity depth, *l*	100 μm
Black chrome thickness, *b*	2500 Å

From Figure 2, it is observed that as *'e'* decreases, sensitivity increases, but FOV decreases; as *'l'* increases, both sensitivity and non-linearity increase.

4. Sensor Fabrication

A Float Zone silicon wafer (p-type, boron-doped) of 10–12 Ω-cm resistivity was used for the fabrication of twin triangular photo detector array. Thermal oxide of 1 μm thick was grown on both sides of the wafer by wet oxidation at 900°C for nine hours. To define the active area of the detectors, triangular windows were opened on the oxide by lithographic patterning. N+/P junction was formed by phosphorus implantation at 80 keV for a dosage of 1×10^{15} ions/cm^2 and subsequent annealing at 850°C for 2 ¼ hrs in forming gas environment to obtain a junction depth of 0.3 – 0.5 μm. A contact pad for the *P*-type was formed by opening rectangular windows on the oxide and deposition of Al by electron beam evaporation. To ensure good ohmic contact with the substrate, alloying of Al with Si was carried out at 450°C in forming gas environment. Ti, Pd, and Ag were deposited sequentially for the metallization of bus bar contact by adopting a lift-off technique. To minimize the reflection from the silicon surface (<5%) in the wavelength region of 500–900 nm, anti-reflection coating using Sub-II (Merck brand) was deposited using electron beam evaporation technique on the active area (Shobha et al., 2011).

Micro-optics were developed on radiation-hardened Schott, make a Corning 7740 wafer of thickness 1000 μm. The wafer was coated with 2500 Å thick Cr on one side, and black chrome on the other. The Cr coating, along with the thick photo resist, acted as an etch mask during the deep glass etching to form the cavity. Rectangular windows were opened for glass etching by lithographic patterning on the Cr. Glass etchant is prepared, using a solution of HF, HCl, NH_4F, and DI water. Wet chemical etching is carried out at 55°C for 120 minutes, to get a cavity depth of around 100 μm, as measured using an optical profiler (Veeco make; Model No. NT-1100-09-436) (Iliescu et al., 2005). During the wet chemical etching, the black chrome was protected by a thick layer of positive photo resist (AZ10XT) baked at 100°C for 45 minutes. Furthermore, a double-side mask aligner (Quintel make) is used to transfer the slit pattern onto the black chrome. Registration accuracy of about ±5 μm is maintained during all stages of lithography. The Pyrex wafer is bonded onto the processed Si wafer by anodic bonding at 380°C applying 1000 V between the electrodes. The devices are diced using a high precision diamond saw (Vectus – 7100, from Advanced Dicing Technologies). The diced chips are packaged onto a four-pin DIP package, and sealed with a top can with an optical window with anti-reflection coating on both sides (Shobha et al., 2011; Ceyssens et al., 2009).

5. Sensor Characterization

Figure 3 shows the packaged micro sun sensor chip, which is characterized for sensor performance. For the characterization of sensitivity, non-linearity, and field of view (FOV), a sun simulator (SESO make) was used.

The micro sun sensor device testing was carried out using the electronic circuit consisting of two separate trans-impedance amplifiers with feedback resistance of 1MΩ for converting current output of the triangular detector to corresponding voltage signal. A summing amplifier (LM124) extracted the SUM signal by adding the outputs of the individual triangular detectors. To normalize the sensor output against the

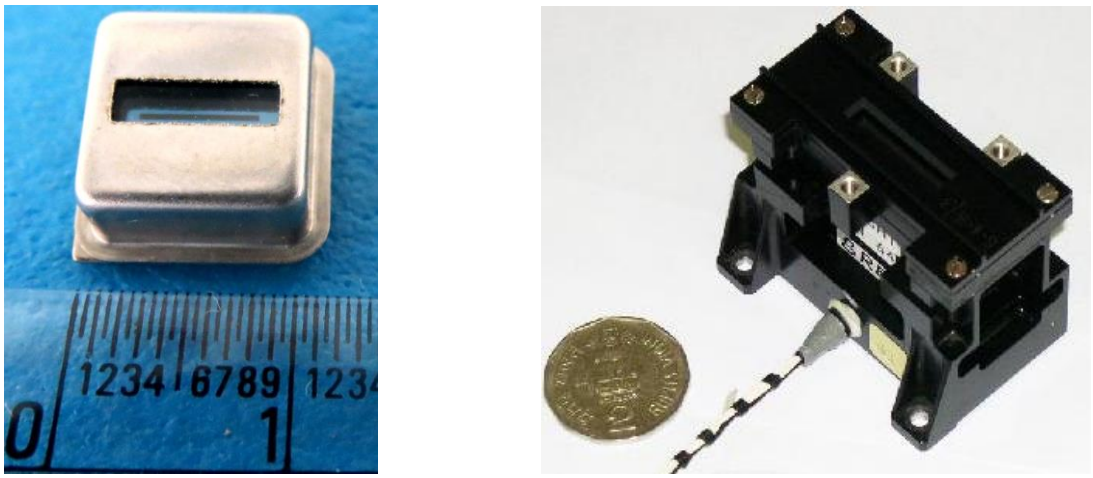

(a) (b)

Figure3. (a) Micro Sun Sensor (size: 12x 12 x 5.5 mm^3); (b) analog sun sensor (size: 58x28x25 mm^3). The micro sun sensor is approximately 50 times smaller than conventionally used analog sun sensors.

ambient variation, a divider (AD534) was used to calculate the ratio of the summed output (SUM) and difference of voltage outputs (DIFF) from the two individual detectors. When the sum of both the detectors crosses a preset threshold, the sun presence (FOV) signal was generated using a fast comparator (LM139). With this circuit (called the test console), performance characterization of the micro sun sensor devices was carried out in front of a sun simulator, which is a Xenon arc lamp simulating Sun intensity equivalent to air mass of 0.02. Keeping the cross axis at 0° (normal to the optical axis), the sensor is then turned by ±45° about the measurement axis on a two-axis Huber rotary aided by two axis stepper motor controllers of resolution 0.1°. For each 0.5° step of rotation, the individual detector output and the processed sensor output (SUM/DIFF) are acquired, using a test console connected to a personal computer with data acquisition software (Shobha et al., 2011). An auto collimator (Nicon make) was used to align the sensor to the center of the sun simulator. These devices were subjected to high energy particle irradiation and their post-radiation sensor performance was studied.

6. Results and Discussion

Prior to irradiation, four devices (MSS03-30, MSS03-40, MSS03-41, and MSS03-46) were initially characterized for their sensitivity, non-linearity, and sun presence (FOV). Results are provided in Figure 4 and Table 2.

6.1. Gamma Irradiation

The devices MSS03-30 and MSS03-46 were subjected to gamma radiation using a *Co-60* source, with a dose of 100 *krad* (rate of ~23 *rad/s*), per the MIL-STD-975. Post-radiation sensor characteristics, namely sensitivity, non-linearity, and sun presence (FOV), were measured, as shown in Figure 5.

Figure 6 shows the overlay of sensor outputs for pre- and post-radiation.

Table 3 shows the values of sensitivity, non-linearity, and sun presence (FOV) for pre-and post-radiation for the devices MSS03-30 and MSS03-46.

From Table 4, it is clear that gamma radiation has very little effect on the performance of the devices, with observed deviations within a measurement error of 2%.

6.2. Electron Irradiation

Devices MSS03-40 and MSS03-41 were subjected to electron irradiation of energy 8-10 MeV with a fluence of 2×10^{13} /cm^2 at RRCAT (Raja Ramanna Centre for Advanced Technology), Indore, India. The irradiation technique used was pulsed electron beam with dual scattering foils. Post-radiation sensor characteristics, namely, sensitivity, non-linearity, and sun pres-

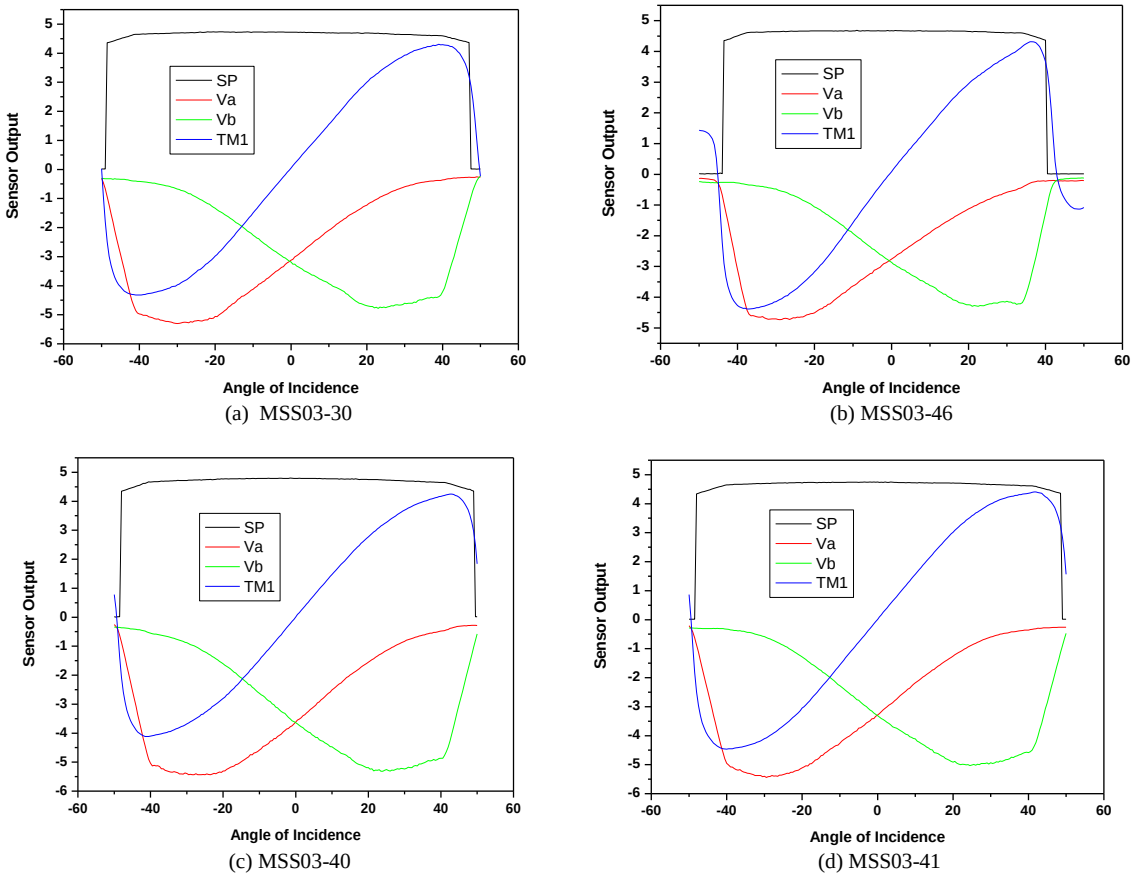

Figure 4.Sensor output plots vs. sun angle incidence in degree; where in SP is sun presence (FOV) signal, Va and Vb are individual outputs from each detector and TM1 is processed sensor output (SUM/DIFF).

Table 2. Sensor Characteristics Prior to Irradiation

SL. No.	Device ID	Sensitivity (mV/deg)	Non-linearity (%) with in FOV 25°	Sun Presence (FOV) (deg)	
				+ axis	– axis
1	MSS03-30	148.4	4.19	48.5	49.0
2	MSS03-40	139.4	5.75	50	48.5
3	MSS03-41	151.6	3.5	49.5	48.5
4	MSS03-46	152.4	3.44	41	44

ence (FOV), were measured. Figure 7 indicates post-radiation tested sensor performance.

Figure 8 shows the overlay of sensor outputs for pre-and post-radiation.

Table 5 shows the values of sensitivity, non-linearity, and sun presence for pre- and post-electron irradiation. It is evident from this table that the sensor performance, mainly non-linearity over ±25°, has deviated from the original value of 3.5% to 6.9% for the device MSS03-41. Similarly, the sun presence FOV is reduced from 50° to 47.5°, and sensitivity (slope) increased from 139 *mV/deg* to *180 mV/deg*, for the device MSS03-40 after the electron irradiation test. The observed non-linearity deviation subsequent to irradiation effect may be attributed to the increase in the reflection from the black chrome-coated slit surface. However, more precise case studies are underway.

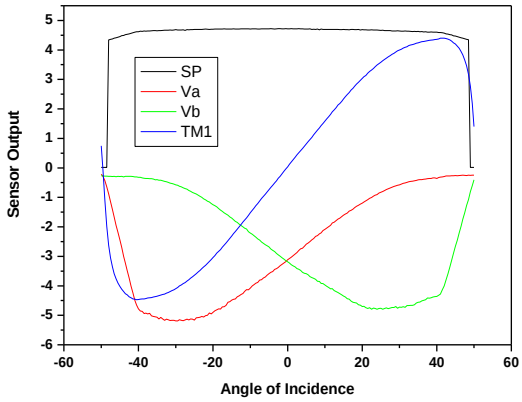

(a) MSS03-30

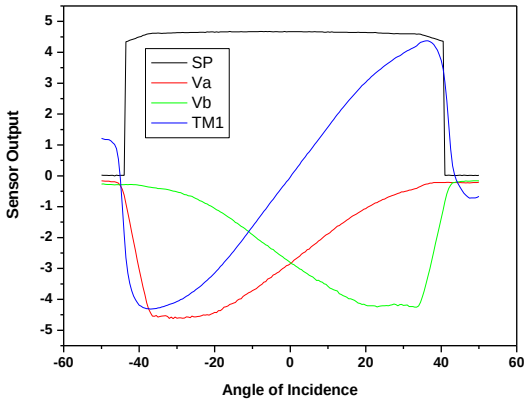

(b) MSS03-46

Figure 5. Sensor outputs after gamma ray irradiation.

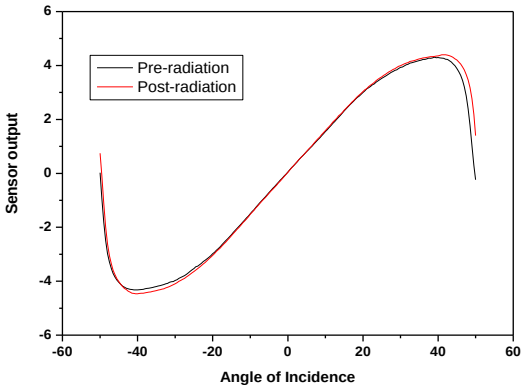

(a) MSS03-30

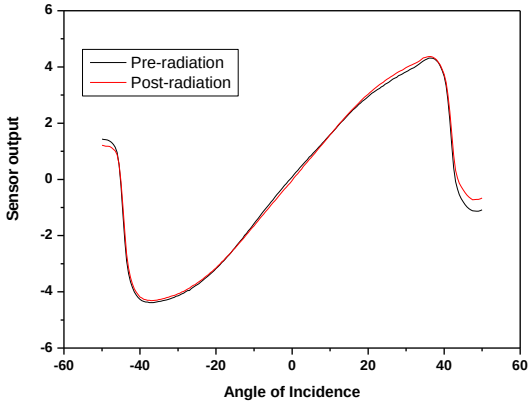

(b) MSS03-46

Figure 6.Sensor outputs for pre- and post-gamma ray radiation.

Table 3. Sensor Characteristics – Pre- and Post-gamma Ray Irradiation

	Device ID			
	MSS03-30		*MSS03-46*	
	Sensitivity (mV/deg)			
Pre	148.4		152.4	
Post	151.1		154.1	
% Deviation	1.81		1.11	
	Non-linearity (%)within FOV 25º			
Pre	4.19		3.44	
Post	3.12		5.32	
Deviation	1.07		1.88	
	Sun presence (FOV) (deg)			
	+ axis	*– axis*	*+ axis*	*– axis*
Pre	48.5	49.0	41	44
Post	49.5	48.5	41	44
Deviation	1	0.5	0	0

Table 4. Individual Detector Outputs at Null

Device ID	Pre-Radiation		Post-Radiation	
	V_A *(V)*	V_B*(V)*	V_A*(V)*	V_B*(V)*
MSS03-30	3.121	3.189	3.116	3.184
MSS03-46	2.755	2.812	2.847	2.808

The maximum reductions in sun presence FOV for MSS03-40 and MSS03-41 are 2.5° and 1.5°, respectively. In the design of micro sun sensor, the sun presence threshold is chosen as 0.8V over FOV ± 50°, but in the electron irradiation experiment, sensor outputs dropped by 47% and 44% for the devices MSS03-40 and MSS03-41 at null (zero degree MFOV and CFOV), as shown in Table 6. This resulted in the reduction of sun presence output below the threshold value of 0.8V at ±50°. Moreover, the discrete data

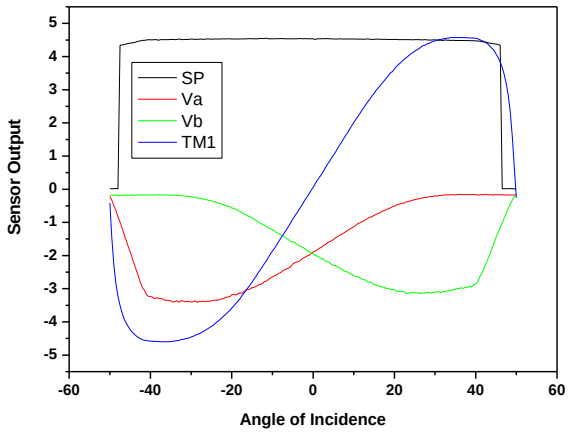

(a) MSS03-40

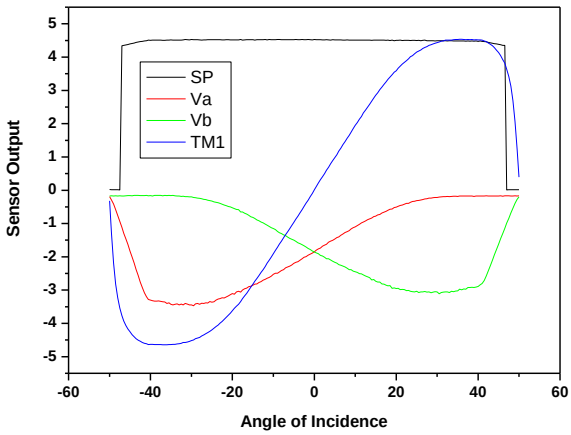

(b) MSS03-41

Figure 7. Sensor outputs for post-electron radiation.

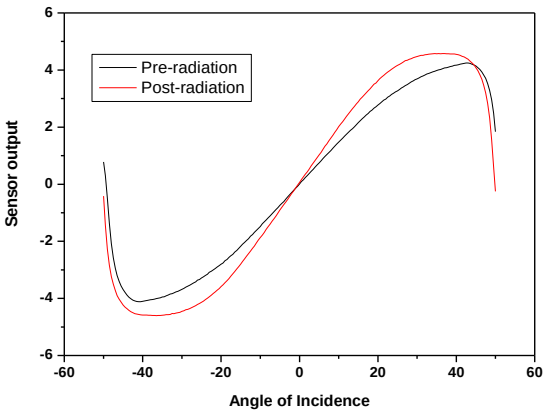

(a) MSS03-40

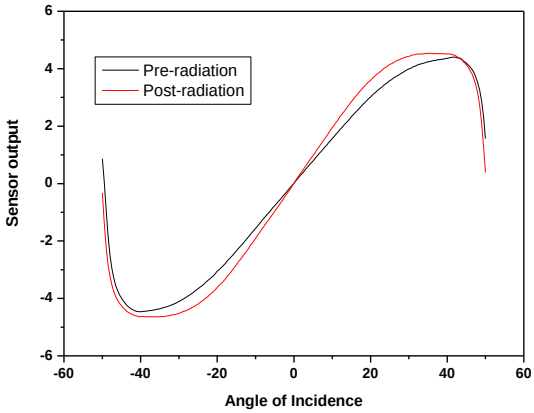

(b) MSS03-41

Figure 8. Sensor outputs for pre- and post-electron radiation.

Table 5. Sensor Performance – Pre- and Post-Electron Radiation

	Device ID			
	MSS03-40		*MSS03-41*	
	Sensitivity (mV/deg)			
Pre	139.4		151.6	
Post	180.3		180.5	
% Deviation	29.3		19.06	
	Non-linearity (%)			
Pre	5.75		3.5	
Post	7.17		6.94	
Deviation	1.42		3.44	
	Sun Presence (deg)			
	+ axis	*– axis*	*+ axis*	*– axis*
Pre	50	48.5	49.5	48.5
Post	47.5	48.5	48	48
Deviation	2.5	0	1.5	0.5

observed for V_A+V_B at 50° indicate the sun presence output values are 0.864V before irradiation and 0.747V at 47.5° after the irradiation test; hence, the 2.5° fall in FOV is mainly due to the fall of the sun presence output value of the twin triangular photo detectors.

The individual detector outputs at null from Table 6 were further analyzed to derive the diffusion length damage coefficient under the electron fluence of 2×10^{13} /cm^2 of energy 8–10 MeV. In the case of electron irradiation, the variation of $(J_o/J)^2$ is linear with respect to the electron flux Φ (Karanth, Sahrma, and Nagendra, 2006), as can be seen from:

$$\left(\frac{J_0}{J}\right)^2 = 1 + L_0^2 K \Phi, \qquad (9)$$

where J_o and J are the short circuit current densities of un-irradiated and irradiated devices, L_o is the diffusion length of the minority carriers of un-irradiated device, and K is the electron damage coefficient (also called diffusion length damage coefficient). Here, diffusion

Table 6. Individual Detector Outputs at Null

Device ID	Pre-Radiation		Post-Radiation		Remarks
	$V_A(V)$	$V_B(V)$	$V_A(V)$	$V_B(V)$	
MSS03-40	3.614	3.643	1.890	1.944	47.16% degradation is observed in $V_A + V_B$ value
MSS03-41	3.282	3.311	1.851	1.856	43.77% degradation is observed in $V_A + V_B$

length L_o is 100 μm for un-irradiated photo detectors of the sensor.

From the quoted *'K'* value 2×10^{-9} (Partain et al., 1995), known L_0 and J_0, their photo currents after irradiation is estimated and found to be reduced by 55% for both devices.

Experimentally observed reduction in their photo currents are 47.16% and 43.77%, respectively, for the devices MSS03-40 and MSS03-41, which is explicit in Table 6. Furthermore, *'K'* value was estimated using experimental results, and was found to be 1.328×10^{-9}, which is in agreement with the theoretical value of 1×10^{-9} (Solar Cell Radiation Handbook, 1989; Mazer, 2011) for 8–10 MeV electrons of fluence 2×10^{13} /cm^2 (Partain et al., 1995).

The observed increase in sensitivity (slope) from 139.4 mV/° to 180.3 mV/°for the device MSS03-40 is due to the reduction in V_A+V_B sum value after irradiation; the factor that is highly sought, after sensor calibration.

7. Conclusion

The development of the micro sun sensor was conducted by synergizing planar silicon photo detector technology with glass micro fabrication technique. The comprehensive design met targeted spacecraft attitude determination sensor specifications, and geometrical parameters of micro sun sensor evolved, while volume was fifty times reduced compared to analog sun sensors. Moreover, the effects of gamma and electron irradiation on the sensor performance were studied. Electron irradiation (8–10 MeV, 2×10^{13} /cm^2) caused performance degradation in the sensors mainly with regard to FOV and non-linearity. Evaluation of onboard performance of first cut prototype devices in the space craft GSAT-19 are expected during the second quarter of 2017.

Acknowledgments

N^+/P diode formation for the present work was carried out at Power Devices, Bharat Electronics, Bengaluru. The authors are thankful to Shri R. Gandhi of Bharat Electronics for the support. Further gamma and electron irradiation was carried out at ISITE, ISRO, Bengaluru, India and RRCAT, Indore. The authors are also grateful to Dr. S. Krishnaveni, Mysore University India, for coordination during electron irradiation testing.

References

Ceyssens, F. and Puers, R. (2009): Deep Etching of Glass Wafers Using Sputtered Molybdenum Masks, *J. Micromech. Microeng.*, Vol. 19, pp. 1–6.

Corning Glass Works Brochure (1987): Corning, NY, 1483.

Hales, J. H. and Pedersen, M. (2002): Two-Axis MOEMS Sun Sensor for Pico Satellites, in *Proc. Annu. Conf. Small Satellites*, Logan, Utah.

Iliescu, C. et al. (2005): Characterization of Deep Wet Etching of Glass, in Device and Process Technologies for Microelectronics, MEMS and Photonics IV, Proc. of SPIE Vol. 6037.

Karanth, S. P., Sharma, S. V. K., and Nagendra, C. L. (2006): Studies on Test and Evaluation of N+-P Junction Silicon Photo Detectors for Space Qualification, *J. Spacecraft Tech.*, Vol. 1, pp. 41–55.

Mazer, J. A. (1987): Solar Cells: An Introduction to Crystalline Photovoltaic Technology: Kluwer Academic.

Partain, L. D. (1995): *Solar Cells and Their Applications*, New York: John Wiley and Sons Inc., pp. 94–123 and Figure 3.5-8.

Pedersen, M., Hales, J. H., and Fleron, R. W.: Linear Two-axis MOEMS Sun Sensor and the Need for MEMS in Space, presented at the 54th International Astronautical Cong., MIC Technical University, Denmark (DTU), Paper AC-03-U.26.02.

Shobha, V. et al. (2011): Design, Fabrication and Characterization Studies on Micro-Electro-Optical Sun Sensor for SpaceCraft Applications, presented at the XXXVOSI Symposium, Thiruvananthapuram.

Solar Cell Radiation Handbook, 3rd ed. (Feb. 1989): JPL publication 82–69.